JGR Oceans

RESEARCH ARTICLE
10.1029/2019JC016042

Eddy-Induced Acceleration of Argo Floats

Tianyu Wang[1,2,3], Sarah T. Gille[4], Matthew R. Mazloff[4], Nathalie V. Zilberman[4], and Yan Du[1,2,3]

[1]State Key Laboratory of Tropical Oceanography, South China Sea Institute of Oceanology, Chinese Academy of Sciences, Guangzhou, China, [2]University of Chinese Academy of Sciences, Beijing, China, [3]Southern Marine Science and Engineering Guangdong Laboratory, Guangzhou, China, [4]Scripps Institution of Oceanography, University of California San Diego, La Jolla, CA, USA

Abstract Float trajectories are simulated using Lagrangian particle tracking software and eddy-permitting ocean model output from the Estimating the Circulation and Climate of the Ocean, Phase II (ECCO2) project. We find that Argo-like particles near strong mean flows tend to accelerate while at their parking depth. This effect is pronounced in western boundary current regions and in the Antarctic Circumpolar Current system. The acceleration is associated with eddy-mean flow interactions: Eddies converge particles toward regions with stronger mean currents. Particles do not accelerate when they are advected by the eddy or mean flow alone. During a 9-day parking period, speed increases induced by the eddy-mean flow interactions can be as large as 2 cm s^{-1}, representing roughly 10% of the mean velocity. If unaccounted for, this acceleration could bias velocities inferred from observed Argo float trajectories.

Plain Language Summary Ocean instruments called floats are carried by ocean currents. Tests carried out using output from a numerical simulation of the ocean show that near strong currents, eddies tend to bump floats into the currents. As a result, on average, at the end of a 10-day sampling period, a float is likely to end up in water that is moving faster than the water where it started 10 days earlier. This effect should be considered when using particles to estimate mean velocities.

Key Points:
- Simulated quasi-Lagrangian particles provide information on the behavior of Argo float trajectories
- Near strong jets and away from the Equator, simulated Argo floats accelerate while at their parking depth
- The acceleration occurs because eddies converge Argo-like floats toward strong currents, even when no Eulerian acceleration occurs

Supporting Information:
- Supporting Information S1

Correspondence to:
S. T. Gille,
sgille@ucsd.edu

Citation:
Wang, T., Gille, S. T., Mazloff, M. R., Zilberman, N. V., & Du, Y. (2020). Eddy-induced acceleration of Argo floats. *Journal of Geophysical Research: Oceans*, *125*, e2019JC016042. https://doi.org/10.1029/2019JC016042

Received 3 JAN 2020
Accepted 1 OCT 2020
Accepted article online 2 OCT 2020

1. Introduction

Velocities measured by Argo floats or other quasi-Lagrangian systems are often assumed to provide unbiased representations of the mean velocity field in the ocean. One of the original objectives in the design of the Argo prototype, Autonomous Lagrangian Circulation Explorers (ALACE), was to provide reference velocities for the hydrographic measurements taken during the World Ocean Circulation Experiment (Davis et al., 1992). Lagrangian trajectories continue to be used as one strategy to determine mean reference geostrophic velocities in the ocean (e.g., Gille, 2003; Gray & Riser, 2014; Wijffels et al., 2001; Zilberman et al., 2017), but success relies on understanding the nature of these trajectories.

There are known challenges to inferring mean geostrophic velocity from Lagrangian particles. One challenge, as noted by Davis (1991), is that particles initially deployed in one patch of the ocean tend to diffuse away from their starting point, giving an illusion of a divergence. To avoid biases related to stochastic divergence, the Argo Program aims to deploy floats relatively uniformly across the globe, and analyses to date have reported no evidence for subsurface divergence or convergence (e.g., Chapman & Sallée, 2017; Gray & Riser, 2014; Ollitrault & Rannou, 2013). A second challenge is that Lagrangian sampling systems that spend significant amounts of time at the ocean surface display patterns of convergence and divergence due to advection by wind-driven ageostrophic Ekman transport. This means, for example, that early Argo floats (which required 12–24 hr at the surface to transmit their data) tended to move off the equator and into regions of strong convergence. In newer deployments, the Argo Program has aimed to mitigate this by making use of Iridium communication systems that allow floats to transmit their data to satellite in about 15 min, thus minimizing displacement at the sea surface and ensuring that trajectory information represents primarily the subsurface motions.

Besides errors incurred while transmitting at the ocean surface, velocities inferred from Argo displacements have the potential to differ from true velocities at the float parking depth for two additional reasons. The first is associated with velocity shear and inertial oscillations in the upper 1,000 m of the water column. During ascent and descent, floats can be displaced relative to water parcels at the parking depth (e.g., Ollitrault &

Rannou, 2013; Park & Kim, 2013; Park et al., 2005). Zilberman et al. (2017) assessed this effect and judged it to be small, albeit worthy of further exploration.

The second reason can occur (even for floats that do not profile) if the floats experience a change in speed while parked. Here we use circulation fields from a numerical model to show that synthetic Argo floats systematically accelerate in the vicinity of mean jets. The magnitude of the accelerations is significant enough to lead to a potential overestimate of current speeds. Our goal is first to characterize the patterns of acceleration and second to identify the mechanisms responsible for the acceleration.

In this paper, section 2 introduces the Argo simulation system and the global synthetic Argo release experiment. Section 3 presents the results from the core Argo simulation, with a focus on the velocity changes along the floats' deep-drifting paths. We identify regions where significant accelerations appear and note that they are colocated with strong mean flows. In section 4 we consider three possible hypotheses to explain the acceleration: (i) the flows in the Estimating the Circulation and Climate of the Ocean, Phase II (ECCO2) model state are spinning up or experiencing a long-term drift; (ii) parking depth trajectories are at constant depth, while water parcels themselves follow isopycnals, and the acceleration is an artifact of examining only the fixed-depth motions; (iii) eddies converge floats into faster mean flows. Section 4 concludes that statistically significant accelerations result from hypothesis III. Section 5 summarizes the major results.

2. Methods and Data Sets

2.1. Modeling Tools

The numerical simulations in this study are aimed at replicating the behavior of Argo floats, which spend most of their time parked at a fixed depth of about 1,000 m and vertically profile every 10 days. Argo floats are not strictly Lagrangian, both because they profile and because they do not follow vertical velocities while parked. In this work we refer to their 1,000-m trajectories as quasi-Lagrangian.

Floats are advected with modeled ocean velocities from ECCO2 (available at http://ecco2.org/; see Menemenlis, Hill, et al., 2005). ECCO2 is an assimilating version of the MITgcm. We use the "Cube 92" solution, which is run on a "cubed sphere" with 18-km (eddy permitting) horizontal grid spacing and 50 vertical levels unevenly distributed between the surface and 6,000 m (Menemenlis et al., 2008). ECCO2 was optimized via Green's function methodology (Menemenlis, Fukumori, et al., 2005) to best represent observed hydrography. ECCO2 fields do not resolve high-frequency or high-wavenumber dynamics, and simulated floats will not be influenced by processes that ECCO2 does not resolve. For the analysis, we use archived 3-day average ECCO2 fields that have been interpolated to a regular 1/4° × 1/4° grid.

Simulated Argo float trajectories are computed using the off-line particle tracking model *Octopus* (see, e.g., Tamsitt et al., 2017; van Sebille et al., 2018; Wang et al., 2018, 2019). *Octopus* retrieves particle velocities from the surrounding eight gridded ECCO2 velocity points at two successive time steps using a trilinear interpolation scheme in space and linear interpolation in time. In our simulation, a 60-s time step is used to integrate the trajectories forward. A uniform horizontal and vertical diffusivity is included to account for dynamics that are unresolved in the ECCO2 fields. The diffusivity has a prescribed value of 10^{-5} m^2 s^{-1}, meaning that its effect is small: a experience small displacements consistent with the net diffusive effect of a random walk while nonetheless primarily following the ECCO2 currents. (See the supporting information for further discussion of the diffusivity.)

2.2. Simulated Argo Float Experiments

For this study, simulated Argo floats are released on a global grid at 0.5° × 0.5° resolution at monthly intervals for a total of 9 years starting 1 October 2005. Octopus computes one full Argo cycle for each simulated float, as illustrated in Figure 1. Simulated floats undergo only one cycle each (in contrast with real Argo floats), since consecutive trajectories might not be statistically independent. Simulated floats are released at Point A. They descend, reaching their parking depth at 1,000 m at Point B (after ~8 hr). After approximately 210 hr at the parking depth, the floats descend from Point C to 2,000 m before rising. At Point D (13 hr after Point C), they reach the ocean surface. Cycle timings for the Argo data were set from average values obtained from the global data centers (ftp://usgodae.org/pub/outgoing/argo or ftp://ftp.ifremer.fr/ifremer/argo). Data from the simulated trajectories analyzed in this work are available online (https://doi.org/10.6075/J0QR4VGP) (Wang et al., 2019).

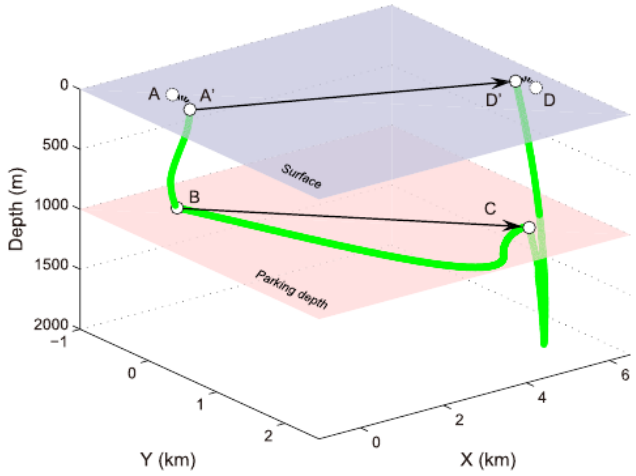

Figure 1. Schematic example of one Argo float cycle. A is the location of the last float fix before leaving the surface (start of the cycle), and A′ is the location where the float starts descending from the surface to parking depth. The float reaches parking depth at Point B, drifts at parking depth to Point C, then starts descending to 2,000 m and measures temperature, salinity, and pressure during ascent to the surface. D′ is the location where the float arrives at the surface. D is the location of the first satellite fix after reaching the surface. (In our numerical simulations, there is no separation from A to A′ or from D′ to D.)

Our analysis uses the parking depth displacements between Points B and C as well as the velocities measured at the start of the displacement at Point B and at the end at Point C. Studies using actual Argo data infer parking depth velocities based on the displacement between surface positions (Point A to Point D) (e.g., Chu et al., 2007; Davis et al., 2001; Gray & Riser, 2014; Lebedev et al., 2007; Ollitrault & Rannou, 2013; Park et al., 2005; Park & Kim, 2013). By using synthetic parking depth trajectories, we avoid a number of biases that are intrinsic to real Argo floats. Floats without Iridium are not always able to obtain position information at the time of descent or ascent, which leads to discrepancies between A (where the float makes its last transmission) and A′ (where it leaves the surface) or correspondingly between D′ and D. (For our simulated calculations A and A′ are the same point, as are D and D′.) Real Argo floats also have biases due to current shear and inertial oscillations that displace floats during descent (Point A to Point B) and ascent (Point C to Point D) (e.g., Ollitrault & Rannou, 2013; Park & Kim, 2013; Park et al., 2005).

2.3. Observed Argo Data and Mapping Method

We use observed Argo trajectories to validate the simulated Argo trajectories and to assess the main results of this study. Several Argo trajectory products have been released (Lebedev et al., 2007; Ollitrault &; Park & Kim, 2013 Rannou, 2013). In this work, we use the ANDRO (Argo New Displacements Rannou and; Park & Kim, 2013 Ollitrault, Ollitrault & Rannou, 2013) data set, which is freely available online (http://www.umr-lops.fr). There are 4,045 Iridium floats with a parking depth of 1,000 m in the ANDRO atlas during the period January 2005 to October 2014. For the purposes of this study, biases induced by using Argo surface positions (e.g., errors from not accounting for vertical shear during ascent and descent), are not considered, as correcting for them is difficult, and the errors are relatively small (e.g., Zilberman et al., 2017) when compared to the mean state. Shear errors would need to be considered to assess acceleration.

We map ANDRO-derived velocities monthly and simulated Argo trajectories using the Cressman interpolation algorithm (Cressman, 1959):

$$\hat{z}(x_0, y_0) = \sum_{i=1}^{n} \lambda_i z(x_i, y_i), \tag{1}$$

where $\hat{z}(x_0, y_0)$ denotes the mapped values on the target grid; $z(x_i, y_i)$ denotes the data and λ_i the weight coefficient that is calculated from:

$$\lambda_i = \frac{\omega_i}{\sum \omega_i}, \tag{2}$$

$$\omega_i = \frac{R^2 - r_i^2}{R^2 + r_i^2}, \tag{3}$$

where R is the interpolating radius, which is here set to 30 km (~1/4°), and only floats within this radius are included in the average. Here $\omega_i > 0$, and r_i is the distance between the target grid center (x_0, y_0; defined on a 1/4° × 1/4° grid for ANDRO and on a 1/2° × 1/2° grid for simulated Argo) and the float position (x_i, y_i; defined as the reported float positions for ANDRO and Point B for synthetic floats). The ANDRO results are further smoothed with a 1/2° × 1/2° moving boxcar average.

3. Synthetic Float Velocities and Accelerations

Average synthetic float velocity magnitudes from Point B to Point C are mapped in Figure 2a. The synthetic float velocities are similar to velocities obtained from real Argo trajectories averaged over the

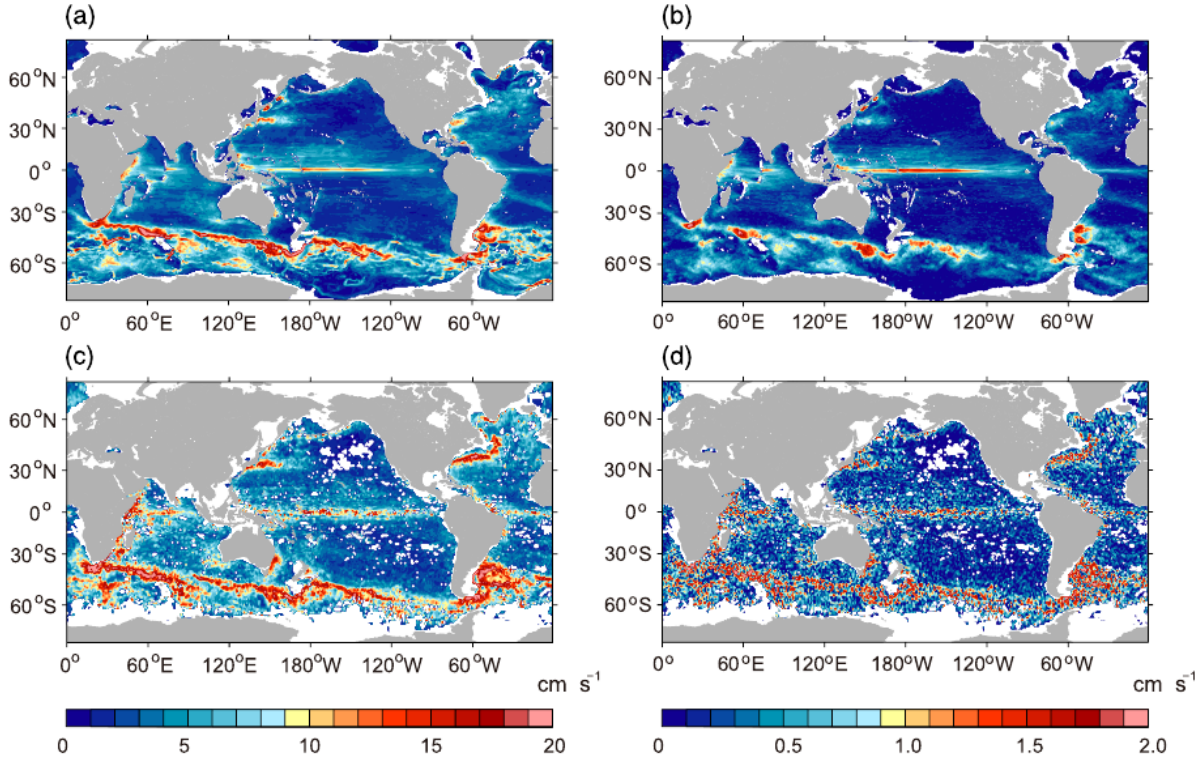

Figure 2. (a) Magnitude of the average velocity, derived from Vectors B and C of simulated Argo floats as $\sqrt{\Delta x^2 + \Delta y^2}/\Delta t$, where Δx and Δy refer to zonal and meridional separations between C and B, in cm, and Δt is the time period between measurements at C and B and (c) from the ANDRO data set during the period from 1 January 2005 to 31 December 2014. The respective uncertainties, which are computed as standard deviation divided by square root of degrees of freedom (here estimated as 108, equivalent to 1 degree of freedom per simulation set) (cm s^{-1}), are shown in (b) and (d).

10-year ANDRO analysis period (from 1 January 2005 to 31 December 2014), shown in Figure 2c. In both cases, high speeds (faster than 10 cm s^{-1}) occur in western boundary current regions, near the equator, and in the Antarctic Circumpolar Current (ACC) system. Uncertainties over this period are computed as standard deviation divided by square root of degrees of freedom (here estimated as 108, equivalent to 1 degree of freedom per simulation set) (Figures 2b and 2d). They show a pattern similar to the mean in which high variability in both fields occurs in the equatorial band, along western boundaries, and in the ACC region. The uncertainties are of comparable magnitude in the model and in ANDRO. Overall, the ECCO2 simulations appear to capture the key features of the observationally inferred 1,000-m depth currents.

To evaluate how velocities change along each quasi-Lagrangian trajectory, we extract the instantaneous horizontal velocity $\mathbf{V}_\mathrm{B}$ at the beginning of the parking depth trajectory (Point B) and horizontal velocity $\mathbf{V}_\mathrm{C}$ at the end of the trajectory (Point C). In our discussion we distinguish between the total derivative $D\mathbf{V}/Dt$ following a Lagrangian particle and the time derivative at a fixed Eulerian point $\partial\mathbf{V}/\partial t$, where formally $D\mathbf{V}/Dt = \partial\mathbf{V}/\partial t + \mathbf{V}\cdot\nabla\mathbf{V}$. Floats themselves are confined to a fixed depth at 1,000 m, so their velocities can be described by $D\mathbf{V_H}/Dt = \partial\mathbf{V_H}/\partial t + \mathbf{V}\cdot\nabla\mathbf{V_H}$, where the H subscript denotes horizontal velocity (and $\mathbf{V}$ is the full three-dimensional velocity).

For each release point on our sampling grid, we compute time-mean speed differences by averaging over the 108 separate particle advection runs. The speed change between drift end and drift start, $|\mathbf{V}_\mathrm{C}|$ minus $|\mathbf{V}_\mathrm{B}|$, shown averaged to the 1/2° × 1/2° release locations (i.e., A points) using the B locations for input r_i in Equation 2, is illustrated in Figure 3a. (Positive numbers denote an increase in speed.) If the horizontal velocities at Points B and C were randomly distributed, we would expect no significant difference in the average speeds. However, accelerations are noted in the Southern Ocean, at the Equator, and in western boundary current regions.

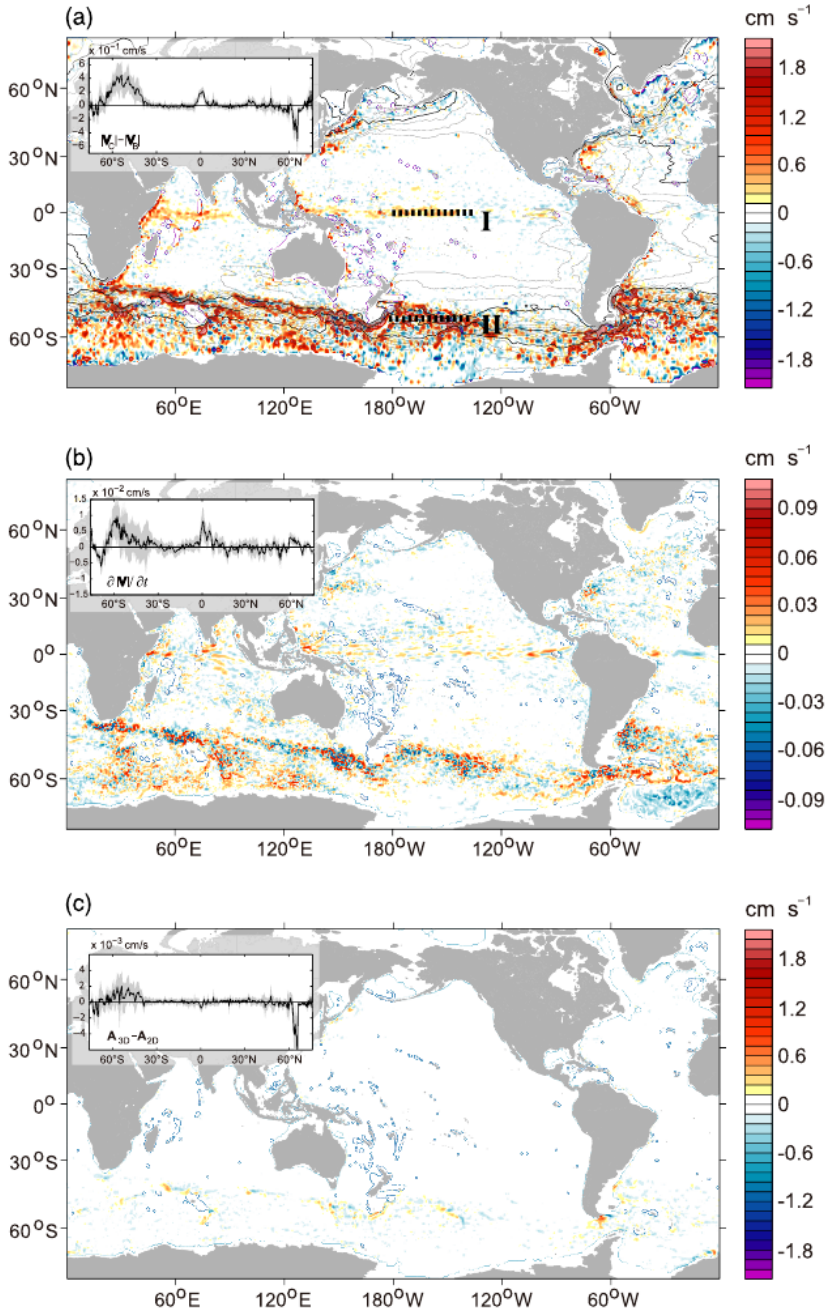

Figure 3. (a) Speed differences between Point B and Point C calculated as $|\mathbf{V}_C|$ minus $|\mathbf{V}_B|$. Sections I (178–132°W, 0°S) and II (178–132°W, 52°S) used in Figure 5 are indicated with black dotted lines. (b) Eulerian speed change at fixed Position B, calculated as $|V_{B|t_C}|-|V_{B|t_B}|$. B denotes the location of parking start (shown in Figure 1), t_B is the parking start time, and t_C is the parking end time. (c) Acceleration obtained with advection by three-dimensional velocity minus acceleration from (a) advecting only with horizontal velocity components. The contours in panel a are the mean pressure isobars at intervals 1,000 N m^{-2} to indicate the ACC. Three representative isobars (-5,000, 0, 5,000) are indicated in bold. Insets in all panels show the zonal average values.

The details of the results depend on the method used to map and average trajectory accelerations. As stated in section 2.3, we map velocities and displacements onto the regular grid associated with the surface Points A using Cressman interpolation with the Point B locations as input r_i in Equation 2. We have also visualized the results by directly averaging all trajectories to their A points. Since the same number of synthetic

floats are started at each Point A, this approach gives equal weight to each geographic location and to each simulated float trajectory. A third approach is to visualize the accelerations by bin averaging at the D points. The accelerations are apparent for all three approaches, and here we show only the Cressman interpolation, as it retains the most fine structure. The most notable difference is at the equator, where accelerations are less apparent for the latter two methods. We hypothesize that this is due to a combination of the fact that the acceleration at the equator in Figure 3a is weak, with limited meridional extent, and the fact that strong shear in the region leads to nonnegligible discrepancies between Locations A and B.

While the acceleration patterns are clear in simulations, verifying model-derived accelerations has not proved feasible with observed Argo float trajectories. ANDRO data cannot provide quasi-Lagrangian velocities at the start ($\mathbf{V}_B$) and end ($\mathbf{V}_C$) of each trajectory, though they can be used to compare trajectory-derived velocities from consecutive cycles, which in principle could demonstrate acceleration patterns if surface motions and vertical velocity shear effects were minimal. However, the ANDRO archive contains only 4,045 Iridium floats from January 2005 to December 2014. In total, these measured an average of ~3.5 trajectories per 0.5° × 0.5° grid cell (though once the Argo array is fully converted to Iridium, they should produce about 10 trajectories per decade per 0.5° × 0.5° grid cell). In contrast, the simulations are based on 108 trajectories at 0.5° × 0.5° spacing. By comparing the mean acceleration ($\overline{|\mathbf{V}_C|-|\mathbf{V}_B|}$) with the standard error of the acceleration ($1.96\,\mathrm{std}(|\mathbf{V}_C|-|\mathbf{V}_B|)/\sqrt{N}$), we estimate that a median of 38 trajectories per grid cell would be needed to infer an acceleration that is statistically significant at the 95% level (see Figures 4a and 4b). The ratio of the number of trajectories needed to the number currently available (see Figure 4c) reveals that approximately 4 times more Argo floats will be needed to infer clear evidence of float acceleration, particularly in highly energetic regions such as the Southern Ocean. In total, the results suggest that another 35 years of Argo data might be needed to infer in situ acceleration patterns on scales consistent with frontal features. These measurement requirements would be reduced if spatial averaging could be increased and would increase if statistical errors in Argo data increased the statistical noise.

Since we do not have sufficient in situ observations to evaluate acceleration, we rely on model results to explore possible mechanisms driving the acceleration. As stated in section 1, we pose three hypotheses for the apparent accelerations in Figure 3a: (i) the flows in the ECCO2 model state are spinning up or experiencing long-term drift; (ii) parking depth trajectories are confined to constant depth, while water parcels themselves follow isopycnals, resulting in accelerations at fixed depth; and (iii) eddies converge floats into faster mean flows.

4. Mechanisms: What Drives Float Acceleration?

4.1. Hypothesis I: The ECCO2 Model State Is Drifting

Long-term model drift can sometimes account for unusual acceleration or deceleration patterns in the deep ocean. In this case, if the acceleration in Figure 3a were an artifact of model spin-up or drift, this would show up in the Eulerian acceleration term, $\partial|\mathbf{V_H}|/\partial t$. However, at 1,000-m depth ECCO2 is statistically in steady state for our analysis period. This is demonstrated by Figure 3b, which shows the average change in speed at fixed Position B, the Eulerian acceleration term $\partial|\mathbf{V_H}|/\partial t$, calculated by $|\mathbf{V}_{\mathrm{B}|t_C}|-|\mathbf{V}_{\mathrm{B}|t_B}|$, where t_B indicates the parking start time and t_C denotes the parking end time. Averaged differences between start and end speeds have a maximum of ±0.09 cm s^{-1}, which is small compared to the change in speed of greater than 2 cm s^{-1} for float trajectories in the Southern Ocean, implying that spin-up cannot account for the observed float behavior.

4.2. Hypothesis II: The Lack of Vertical Advection of Argo Floats Results in Acceleration

Float acceleration at 1,000-m depth, $D|\mathbf{V_H}|/Dt$, might be hypothesized to result from the two-dimensional framework, with an expectation that the acceleration would disappear if we considered three-dimensional, fully Lagrangian particle motions. To assess this, we repeated the analysis from section 3 using the full three-dimensional velocity, including vertical velocity advection. The results differed from the horizontal advection case by less than 1% (Figure 3c), indicating that the observed acceleration is not an attribute of fixed-depth particles only.

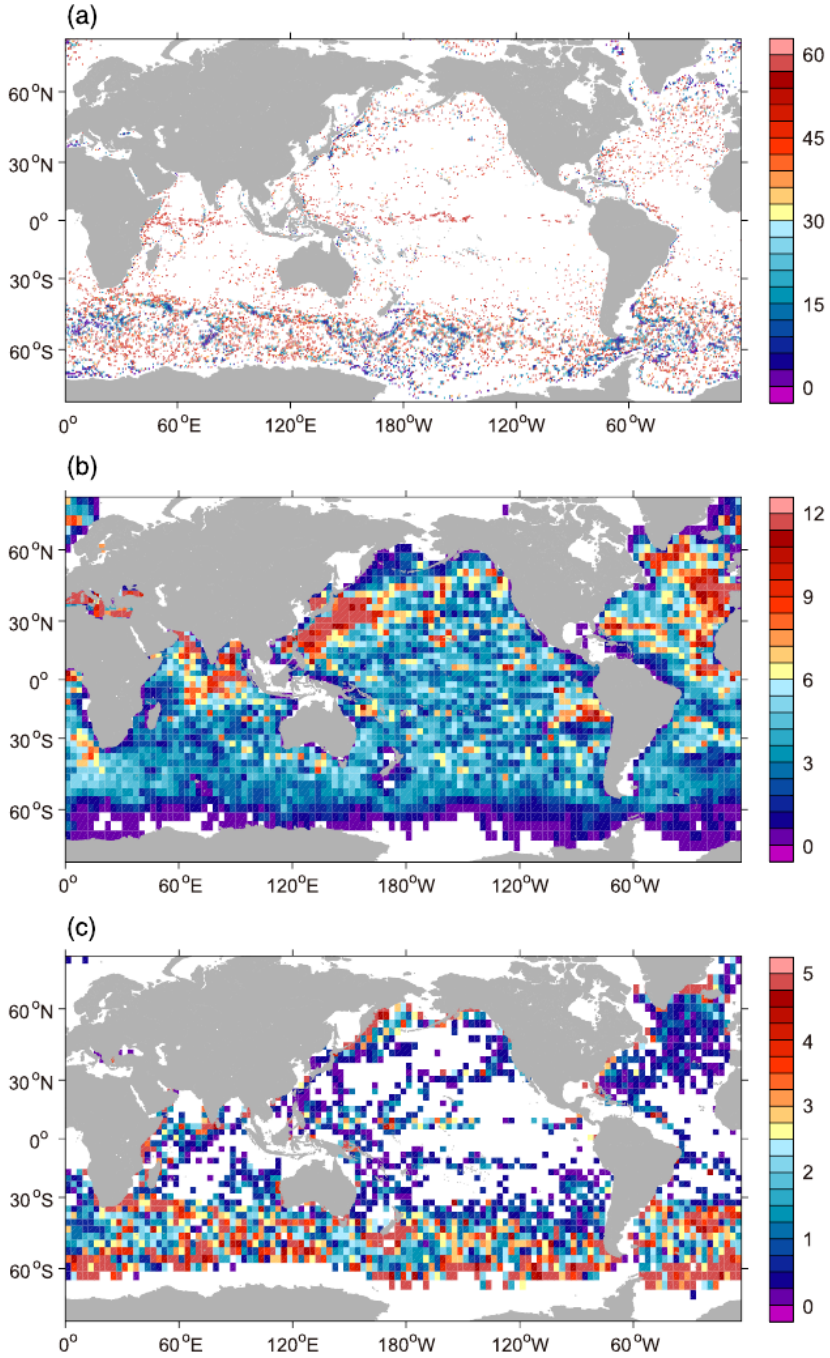

Figure 4. (a) Number of trajectories required to determine a statistically significant float acceleration, as inferred from 108 simulations spaced at 0.5° × 0.5° grid resolution. See text for calculation procedure. Pixels are white if acceleration is not statistically significant at the 95% significance level. (b) Average number of Argo float trajectories transmitted by Iridium available in a 0.5° × 0.5° grid box for the time period from January 2005 through December 2014, plotted as 3° × 3° averages. The number of float trajectories measured by Argo is roughly a factor of 10 smaller than the number that would be needed to detect statistically significant acceleration at the grid scale. (c) The ratio between (a) and (b), plotted as 3° × 3° averages.

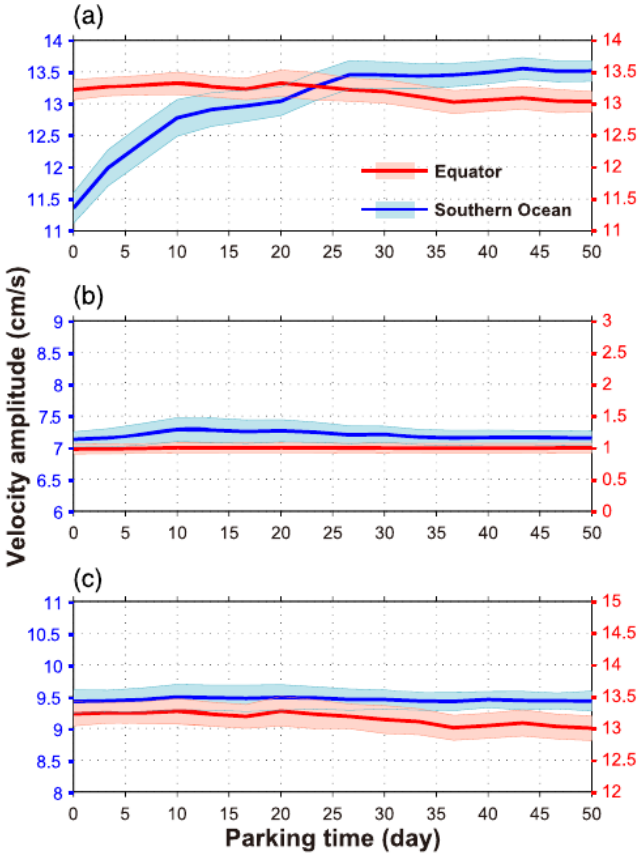

Figure 5. The speed of simulated floats during the parking phase derived from (a) the full input velocity field, (b) the mean field, and (c) the eddy field. Every 30 days, 1,000 simulated floats are released at the target locations (equatorial section and the Southern Ocean section; see Lines I and II in Figure 3a). With 100 total releases, the lines represent the mean of 100,000 simulated floats. Results from the equatorial region are in red, and Southern Ocean results are in blue. Shaded envelopes indicate uncertainties representing the 95% confidence intervals based on the standard error of the mean. These are computed using 1,000 realizations of a bootstrapping procedure (Dicicco & Efron, 1996).

4.3. Hypothesis III: Eddies Converge Floats Into Faster Mean Flows

4.3.1. Eddy-Mean Flow Interaction

Modeling studies using quasi-geostrophic models (e.g., Williams et al., 2007; Wolff et al., 1991) and full general circulation models (e.g., Stewart et al., 2019) have revealed that jets are maintained by eddy-mean flow interactions, with eddies acting to accelerate the jet centers while extracting momentum from the wings of the jets. In the real ocean, eddy statistics derived from altimetry have also provided evidence that eddies accelerate jets where eddy effects are most intense (e.g., Morrow et al., 1992, 1994; Qiu & Chen, 2010; Stewart et al., 2015). In this way eddies can act like a negative viscosity (e.g., Starr, 1968; Marshall et al., 2012). Thus, our third hypothesis is that floats accelerate while parked because eddy motions converge them into regions of faster mean flows.

To test specifically whether the acceleration results from eddy-mean flow interaction, we carry out numerical experiments in which we assess float speed as a function of parking period from 0 to 50 days for two test regions (indicated in black in Figure 3a): Section I (178–132°W, 0°S) is located along the equator, and Section II (178–132°W, 52°S) along the ACC in the Southern Ocean. The experiments at each location use a total of 100 releases spaced at time intervals of 30 days, with 1,000 floats simulated in each release, initially spaced at 0.05° intervals. Floats released along the equator accelerate by approximately 0.2 cm s^{-2} over the first 10 days in consistency with Figure 3a, but here we can see that it is statistically insignificant (red lines in Figure 5a). In contrast, floats in the Southern Ocean speed up by approximately 2 cm s^{-2}, a 15% acceleration, within the first 26 parking days (blue lines in Figure 5a). This 26-day timescale is suggestive of the influence of mesoscale dynamics.

We test the hypothesis that eddies are responsible for the float acceleration by carrying out additional experiments in which simulated quasi-Lagrangian floats are advected either by the 10-year time-mean velocities $(\bar{u}, \bar{v})$ or by "eddy-only" velocities (u', v'). Results, in Figures 5b and 5c, show no evidence for acceleration in either case, regardless of parking time. With the mean flow, the average particle speeds ($|\mathbf{V}_{\text{mean}}|$) are about 1.0 cm s^{-1} at the equator and 7.2 cm s^{-1} in the Southern Ocean. In contrast, when the floats are advected by eddies only, we find mean eddy speeds ($|\mathbf{V}_{\text{eddy}}|$) of about 13.1 cm s^{-1} at the equator and 9.5 cm s^{-1} in the Southern Ocean. (Formally, the mean and eddy components do not sum to produce the total speed because we are examining averaged speed, computed by first determining speed and then averaging rather than averaging velocity squared and then taking a square root to obtain a representative speed. In the kinetic energy budget discussed in section 4.3.2, mean and eddy components do sum to total kinetic energy.)

The 10-year mean used for Figures 5b and 5c implies that the eddy component of the flow includes variability ranging from rapidly evolving transient eddies to long-term displacements of the ACC to interannual variability. As an alternative, we also carried out the calculations for Figure 5 using monthly means. This resulted in a slightly less energetic mean and slightly more energetic eddy transports, as one would expect, but results were the same within error bars (not shown), implying that the results found here are largely governed by eddy variability that occurs on timescales of less than a month.

To evaluate whether floats uniformly accelerate in the Southern Ocean, we assess change in speed during each trajectory ($|\mathbf{V}_C|$ minus $|\mathbf{V}_B|$) within boxes centered at the latitude of the core of the ACC jets (defined by the latitude of the maximum zonal mean velocity in ECCO2) and extending ±2.5° in latitude. Each

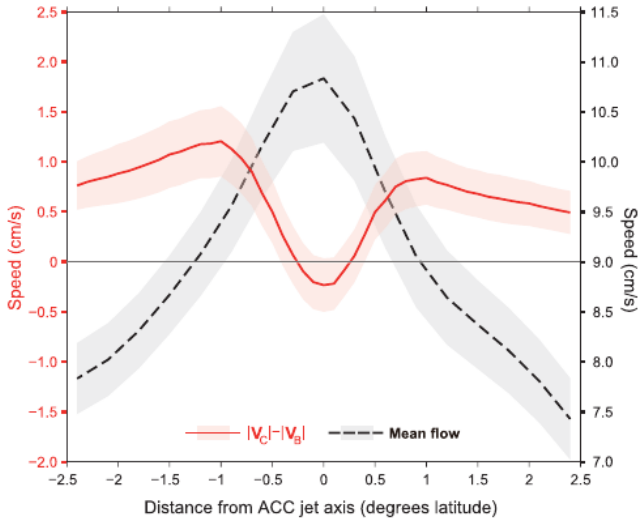

Figure 6. Along-ACC averaged speed changes (calculated from $|\mathbf{V}_C|$ minus $|\mathbf{V}_B|$ as shown in Figure 3a) for floats released in the ACC region (see text for details), plotted as a function of distance from the ACC core. Here the core is defined by the latitude of the maximum zonal velocity. The red line indicates the median acceleration, and the red shading indicates uncertainties representing the 95% confidence intervals computed from the standard error of the mean, using 1,000 realizations of a bootstrapping procedure. The dashed overlaid black line and the gray shading indicate the mean speeds and the associated uncertainties in this same coordinate system.

box is 0.5° wide in longitude, yielding 720 total boxes. This analysis is based on the global release experiment described in section 2.2, in which we repeat releases at 30-day intervals over the 2005 to 2014 simulation period, producing 108 simulations. We then average speed changes as a function of Point B distance from the core of the ACC jets (red line in Figure 6). The synthetic floats that we analyze are distributed roughly symmetrically about the ACC jet axis and are representative of the full circumpolar longitude range. Results in Figure 6 show net deceleration (albeit modest in magnitude) within a narrow band (±0.3°) about the jet axis. Everywhere else, we see evidence of acceleration. This shows that on average, while some floats that start in regions of strong flow decelerate, floats on the flanks of the ACC generally accelerate. For perspective, the black line in Figure 6 shows the mean jet speed in this same distance-from-the-ACC-core coordinate system. Though averaging significantly smooths the ACC current system structure and the sharpness of the fronts, we see that in the flanks of the ACC the mean speed at 1,000 m rapidly changes from ~8 cm s^{-1} at 1.5° from the core to ~10 cm s^{-1} at 0.5° from the core. These findings are all consistent with the hypothesis that floats are being fluxed into jet cores by eddies, analogous to how eddies flux momentum from the flanks into the jet cores.

4.3.2. Float Convergence and the Energy Budget

An additional set of experiments was carried out to examine float convergence into mean jets. Synthetic floats were deployed at 30-day time intervals, with a spatial resolution of 0.25° and at 30-day time intervals meaning there were 108 deployments per location. The floats were advected by the full velocity field and configured to remain at the parking depth for 50 days. The final distribution of the float array indicates the large-scale effect of mesoscale eddies working together with mean flows. We quantify this horizontal float distribution using a discretized two-dimensional density of floats, normalized relative to the initial distribution (Figure 7a) denoted

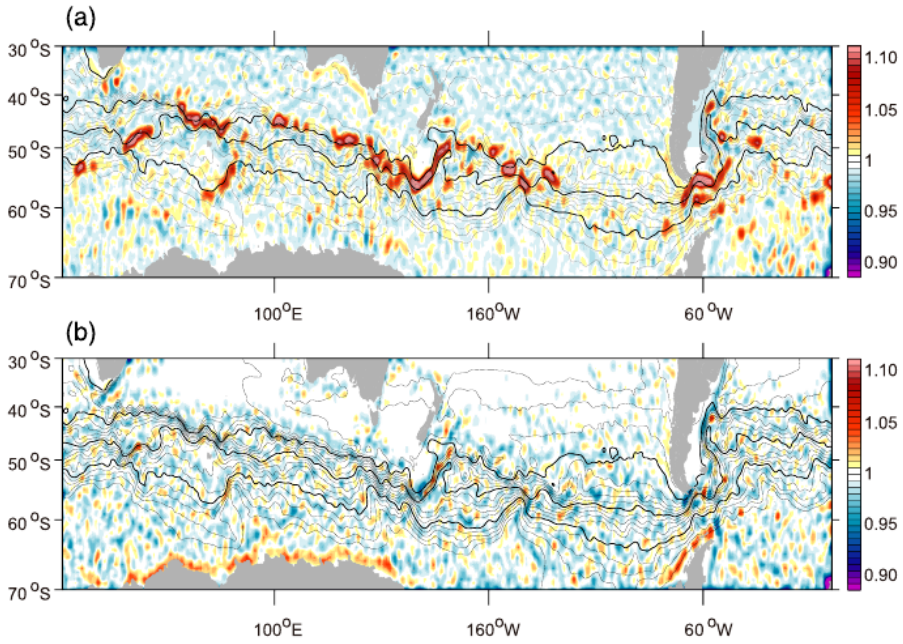

Figure 7. (a) The two-dimensional density of the ECCO2-derived synthetic Argo floats on Day 20, normalized relative to the initial distribution. Values of 1 indicate that the final float density in a 0.25° × 0.25° box is the same as the initial float density. (b) Similar to (a) but with advection carried out using only the mean flow in order to remove eddy effects. Contours indicate mean pressure isobars, as in Figure 6.

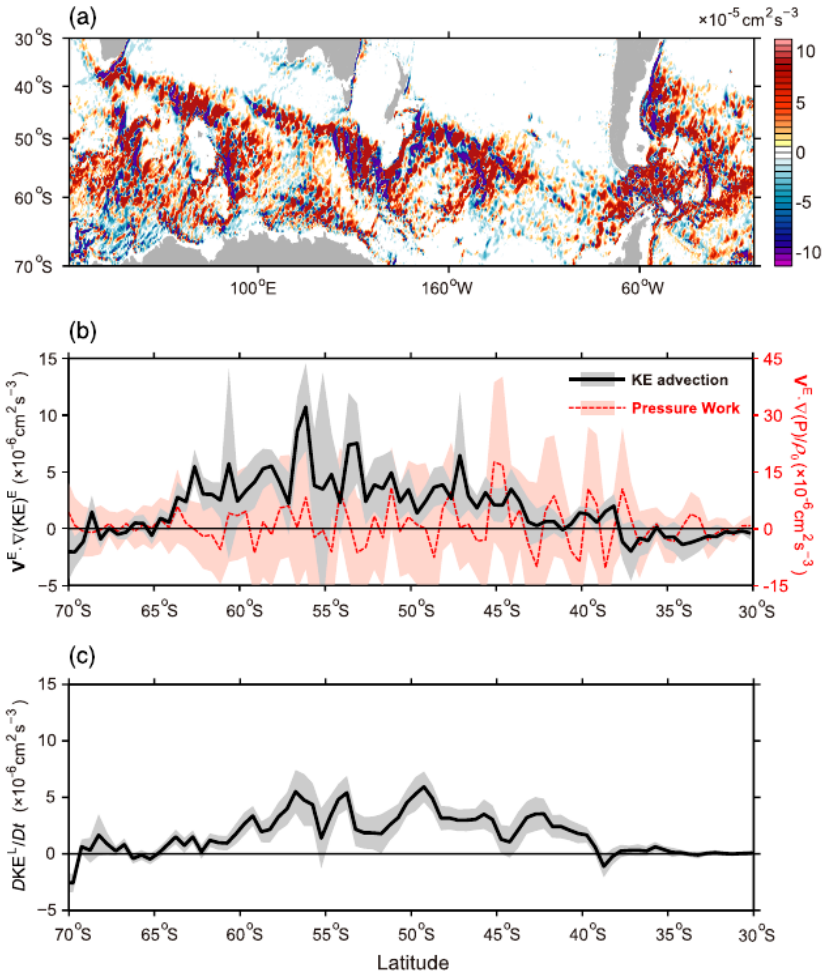

Figure 8. (a) Total derivative of kinetic energy, inferred from advection term ($D\mathrm{KE}/Dt \approx \mathbf{V_H} \cdot \nabla \mathrm{KE}$, with the assumption that the Eulerian tendency term, $\partial \mathrm{KE}/\partial t$ is negligible). The Eulerian fields are computed from ECCO2 over the time period from 2005–2014. (b) Zonally averaged KE advection term from panel (a) (black line). The red line shows the zonally averaged pressure work term. Uncertainties are computed as zonal standard deviation (σ) divided by square root of degrees of freedom (here estimated as 720, equivalent to one independent point per two model grid points = 0.5° longitude). (c) Zonally averaged quasi-Lagrangian total derivative of KE ($D\mathrm{KE}/Dt$) from synthetic floats, estimated as $\frac{1}{2}(\mathbf{V_C}^2 - \mathbf{V_B}^2)/(t_C - t_B)$. Uncertainties represent the 95% confidence intervals based on 1,000 bootstrapped standard deviations.

as $\rho(x, y, \mathrm{T})$, where x and y indicate geographic coordinates and T represents the elapsed time. This function counts the number of floats at time T that are within a 0.25° × 0.25° grid box centered at (x, y) and normalizes by the original number of floats. For example, $\rho(x_0, y_0\ 0\mathrm{d}) = 1$ is the original density, and $\rho(x_0, y_0, 10\mathrm{d}) = 1.2$ indicates that the number of floats within this grid box (x_0, y_0) has increase by 20% after 10 days. Figure 7a shows the normalized density of floats at Day 20, which captures the period of the most significant acceleration (Figure 4a). High values of the density function in jets imply convergence. The results show that over the 20-day trajectories the floats have converged into the jets and encountered faster mean flows. Eddies play a critical role in driving this convergence: We find no convergence when we repeat these experiments advecting the synthetic floats only with the time-mean component of the velocity (Figure 7b).

To further explore the underlying dynamics, we consider the kinetic energy (KE), where KE is $\frac{1}{2}|\mathbf{V_H}|^2$ (i.e., representing horizontal kinetic energy only). By computing the dot product of $\mathbf{V}_H$ and $D\mathbf{V_H}/Dt$, we obtain a kinetic energy equation: $D\mathrm{KE}/Dt = \partial \mathrm{KE}/\partial t + \mathbf{V_H} \cdot \nabla \mathrm{KE} + w\partial \mathrm{KE}/\partial z$. Since ECCO2 is in

statistically steady state, the Eulerian time derivative term, $\partial KE/\partial t$, is negligible (similar to Figure 3b), and the vertical advection term, $w\partial KE/\partial z$, is also negligible (not shown here, but related to Figure 3c). Thus, the Lagrangian change in KE is attributed to horizontal advection: $DKE/Dt \approx \mathbf{V_H} \cdot \nabla KE$. In Figure 8a, the time-averaged advection of KE over the Southern Ocean (from ECCO2 simulated floats) is predominantly positive (red), consistent with increasing KE along quasi-Lagrangian particle pathways, as inferred from Figure 3a. Although Figure 8a shows some negative patches (blue), the zonal average indicates that the advective terms act to increase KE in the latitude band between 38°S and 65°S, with a maximum in the core of the ACC jets, around 56°S (Figure 8b). The zonally averaged advection of KE in Figure 8b is largely consistent with the zonally averaged increase in KE along quasi-Lagrangian pathways (Figure 8c), computed as $\frac{1}{2}(|\mathbf{V_H}|_C^2 - |\mathbf{V_H}|_B^2)/(t_C - t_B)$. The consistency between the black lines in Figures 8b and 8c implies that the float acceleration can be largely represented through advection, which encompasses eddy-mean flow interactions.

The KE framework provides a straightforward means to ask how there can be quasi-Lagrangian acceleration ($DKE/Dt \neq 0$) but no Eulerian acceleration ($\partial KE/\partial t \approx 0$). This is due to the fact that there are substantial sources and sinks of KE in the ocean. The ACC receives a major input of KE due to wind power input (Roquet et al., 2011) and from potential energy conversion via baroclinic instability (Johnson & Bryden, 1989). Meanwhile, the ACC also has major sinks of energy due to dissipation and pressure work. We thus hypothesize that in the core of the ACC these sinks are greater than the sources and must balance KE advection in order to sustain the ACC. At 1,000-m depth, the pressure work term $(\rho_\circ^{-1}(up_x + vp_y))$ is expected to be a major contributor to the energy balance. Pressure work computed from the 3-day averaged ECCO2 fields regridded to 0.25° × 0.25° resolution (red line in Figure 8b) is of the same order of magnitude as kinetic energy advection but does not have the same structure as the KE advection, suggesting that the ECCO2 kinetic energy balance may depend on KE contributions from the high-frequency pressure and velocity terms that are not archived and possibly from the high-wavenumber signals that are lost in the regridding process. A more definitive assessment of the energetic balances would require targeted model experiments that archived all relevant terms.

5. Discussion and Conclusions

In this study we have used a synthetic Argo float simulation system to show that floats tend to accelerate near strong jets while at the 1,000-m parking depth. The acceleration is noticeable in regions of high eddy energy, including western boundary currents and the ACC system. On average, float speed at the parking depth in the ACC increases with parking duration, up to approximately 25 days, which is longer than the standard 9-day parking period used by the Argo program (Roemmich et al., 1998). Our results suggest that during this 9-day parking period, floats located near the ACC may increase their speeds by ~2 cm s^{-1}. Efforts to determine 1,000 m ocean velocities from Argo trajectories should take the impact of these accelerations into account.

The acceleration is not a result of model spin-up, as simulated ECCO2 currents are statistically steady (i.e., $\partial \mathbf{V}/\partial t \approx 0$). Moreover, it is not a side-effect of examining only horizontal velocities at the parking depth. In addition eddies alone do not accelerate quasi-Lagrangian particles: A control experiment, in which simulated floats are advected by "eddy-only" velocities, shows no acceleration of synthetic floats. Diagnosed eddy-induced convergence and kinetic energy imply that the acceleration results from convergence into mean jets arising from eddy-mean flow interactions and as a result of the advective terms. These findings have implications for understanding the dynamics of eddy-jet interactions in the real ocean.

While this acceleration should be considered when inferring 1,000-m ocean velocities from float positions, it is not the only source of potential biases. Preliminary results suggest that shear errors can also result in differences in inferred velocities of up to 2 cm s^{-1}, that is, 10% near the equator and in some western boundary currents (see supporting information Figure S1), implying that acceleration and shear should both be considered near strong currents.

A significant caveat of this work is that the ECCO2 solution has a resolution of approximately 18 km and thus only partially resolves eddies. Moreover, the floats are advected by 3-day average ECCO2 velocities, so we cannot assess the impact of higher frequency dynamics. The sensitivity of our results to model

resolution and high-frequency dynamics should be investigated. A dedicated process experiment using a higher-resolution model to consider this acceleration, perhaps in a controlled setting, would be beneficial for fully elucidating the dynamics. Actual float trajectories might also help to quantify the convergence predicted in our study. However, our results suggest that at current Argo spacing, several more decades of trajectory data will be needed to map statistically significant acceleration patterns at the scale of mesoscale frontal features in the ocean. While caveats exist, the work here suggests that the acceleration of floats while parked can be significant enough that it should be considered both in planning float deployment strategies and in mapping mean middepth ocean currents from Argo trajectories.

Data Availability Statement

Simulated trajectory data used in this analysis are available online (https://doi.org/10.6075/J0QR4VGP). Output from ECCO2 (i.e., Cube 92) is available online (https://ecco-group.org/products.htm). The Argo data used here (field 42281 from http://doi.org/10.17882/42182) were collected and made freely available by the International Argo Program and by the national programs that contribute to it. The ANDRO data set is available online (http://www.umr-lops.fr).

Acknowledgments

We thank Jinbo Wang for helpful input. T. W. and Y. D. are partially supported by the National Natural Science Foundation of China (41525019, 41830538), the Chinese Academy of Sciences (XDA15020901, 133244KYSB20190031), and the Southern Marine Science and Engineering Guangdong Laboratory (Guangzhou) (GML2019ZD0303, 2019BT2H594). S. T. G. and M. R. M. received support from the National Science Foundation through Grants OCE-1234473, PLR-1425989, and OPP-1936222. N. Z. was supported by the National Oceanic and Atmospheric Administration Grant NA14OAR4310219 and by CIMEC Grant NA15OAR4320071, which also supports the Scripps Institution of Oceanography's participation in U.S. Argo (NOAA Climate Program Office FundRef 100007298.)

References

Chapman, C. C., & Sallée, J.-B. (2017). Can we reconstruct mean and eddy fluxes from Argo floats? *Ocean Modelling*, *120*, 83–100. https://doi.org/10.1016/j.ocemod.2017.10.004

Chu, P. C., Ivanov, L. M., Melnichenko, O. V., & Wells, N. C. (2007). On long baroclinic Rossby waves in the tropical North Atlantic observed from profiling floats. *Journal of Geophysical Research*, *112*, C05032. https://doi.org/10.1029/2006JC003698

Cressman, G. P. (1959). An operational objective analysis system. *Monthly Weather Review*, *87*(10), 367–374. https://doi.org/10.1175/1520-0493(1959)087<0367:AOOAS>2.0

Davis, R. E. (1991). Observing the general circulation with floats. *Deep Sea Research Part A*, *38*, S531–S571. https://doi.org/10.1016/S0198-0149(12)80023-9

Davis, R. E., Sherman, J. T., & Dufour, J. (2001). Profiling ALACEs and other advances in autonomous subsurface floats. *Journal of Atmospheric and Oceanic Technology*, *18*(6), 982–993. https://doi.org/10.1175/1520-0426

Davis, R. E., Webb, D. C., Regier, L. A., & Dufour, J. (1992). The Autonomous Lagrangian Circulation Explorer (ALACE). *Journal of Atmospheric and Oceanic Technology*, *9*, 264–285. https://doi.org/10.1175/1520-0426(1992)009<0264:TALCE>2.0.CO;2

Diciccio, T. J., & Efron, B. (1996). Better bootstrap confidence intervals. *Journal of the American Statistical Association*, *11*(3), 189–228. https://doi.org/10.2307/2289144

Gille, S. T. (2003). Float observations of the Southern Ocean. Part I: Estimating mean fields, bottom velocities, and topographic steering. *Journal of Physical Oceanography*, *33*(6), 1167–1181. https://doi.org/10.1175/1520-0485(2003)033<1167:FOOTSO>2.0.CO;2

Gray, A. R., & Riser, S. C. (2014). A global analysis of Sverdrup balance using absolute geostrophic velocities from Argo. *Journal of Physical Oceanography*, *44*, 1213–1229. https://doi.org/10.1175/JPO-D-12-0206.1

Johnson, G. C., & Bryden, H. L. (1989). On the size of the Antarctic Circumpolar Current. *Deep Sea Research Part A Oceanographic Research Papers*, *36*(1), 39–53. https://doi.org/10.1016/0198-0149(89)90017-4

Lebedev, K. V., Yoshinari, H., Maximenko, N. A., & Hacker, P. W. (2007). Velocity data assessed from trajectories of Argo floats at parking level and at the sea surface. *IPRC Technical Note*, *4*(2), 1–16.

Marshall, D. P., Maddison, J. R., & Berloff, P. S. (2012). A framework for parameterizing eddy potential vorticity fluxes. *Journal of Physical Oceanography*, *42*, 539–557. https://doi.org/10.1175/JPO-D-11-048.1

Menemenlis, D., Campin, J.-M., Heimbach, P., Hill, C., Lee, T., Nguyen, A., et al. (2008). ECCO2: High resolution global ocean and sea ice data synthesis. *Mercator Ocean Quarterly Newsletter*, *31*, 13–21.

Menemenlis, D., Fukumori, I., & Lee, T. (2005). Using Green's functions to calibrate an ocean general circulation model. *Monthly Weather Review*, *133*(5), 1224–1240. https://doi.org/10.1029/2005EO090002

Menemenlis, D., Hill, C., Adcroft, A., Campin, J.-M., Cheng, B., Ciotti, B., et al. (2005). NASA supercomputer improves prospects for ocean climate research. *Eos, Transactions American Geophysical Union*, *86*(9), 89–96. https://doi.org/10.1175/MWR2912.1

Morrow, R., Church, J., & Coleman, R. (1992). Eddy momentum flux and its contribution to the Southern Ocean momentum balance. *Nature*, *357*(6378), 482–484. https://doi.org/10.1038/357482a0

Morrow, R., Coleman, R., Church, J., & Chelton, D. (1994). Surface eddy momentum flux and velocity variances in the Southern Ocean from Geosat altimetry. *Journal of Physical Oceanography*, *24*, 2050–2071. https://doi.org/10.1175/1520-0485(1994)024,_2050:SEMFAV.2.0.CO;2

Ollitrault, M., & Rannou, J. P. (2013). ANDRO: An Argo-based deep displacement dataset. *Journal of Atmospheric and Oceanic Technology*, *30*(4), 759–788. https://doi.org/10.1175/JTECH-D-12-00073.1

Park, J. J., & Kim, K. (2013). Deep currents obtained from Argo float trajectories in the Japan/East Sea. *Journal of Atmospheric and Oceanic Technology*, *85*, 169–181. https://doi.org/10.1016/j.dsr2.2012.07.032

Park, J. J., Kim, K., King, B. A., & Riser, S. C. (2005). An advanced method to estimate deep currents from profiling floats. *Journal of Atmospheric and Oceanic Technology*, *22*(8), 1294–1304. https://doi.org/10.1175/JTECH1748.1

Qiu, B., & Chen, S. (2010). Eddy-mean flow interaction in the decadally modulating Kuroshio Extension system. *Deep-Sea Research*, *57*, 1098–1110. https://doi.org/10.1016/j.dsr2.2008.11.036

Roemmich, D., Boebel, O., Freeland, H., King, B., LeTraon, P.-Y., Molinari, R., et al. (1998). On the design and implementation of Argo—An initial plan for a global array of profiling floats. International CLIVAR project Office ICPO Report No.21. GODAE Report No 5. Published by the GODAE International Project office, c/o Bureau of Meteorology, Melbourne, Australia, 32pp.

Roquet, F., Wunsch, C., & Madec, G. (2011). On the patterns of wind-power input to the ocean circulation. *Journal of Physical Oceanography*, *41*(12), 2328–2342. https://doi.org/10.1175/JPO-D-11-024.1

Starr, V. P. (1968). *Physics of negative viscosity phenomena* (p. 224). New York: McGraw-Hill Book Company.

Stewart, A. L., Klocker, A., & Menemenlis, D. (2019). Acceleration and overturning of the Antarctic Slope Current by winds, eddies, and tides. *Journal of Physical Oceanography*, *49*(8), 2043–2074. https://doi.org/10.1175/JPO-D-18-0221.1

Stewart, K. D., Spence, P., Waterman, S., Sommer, J. L., Molines, J.-M., Lilly, J. M., & England, M. H. (2015). Anisotropy of eddy variability in the global ocean. *Ocean Modelling*, *95*, 53–65. https://doi.org/10.1016/j.ocemod.2015.09.005

Tamsitt, V., Drake, H. F., Morrison, A. K., Talley, L. D., Dufour, C. O., Gray, A. R., et al. (2017). Spiraling pathways of global deep waters to the surface of the Southern Ocean. *Nature Communications*, *8*, 172. https://doi.org/10.1038/s41467-017-00197-0

van Sebille, E., Griffies, S. M., Abernathey, R., Adams, T. P., Berlof, P., Biastoc, A., et al. (2018). Lagrangian ocean analysis: Fundamentals and practices. *Ocean Modelling*, *121*, 49–75. https://doi.org/10.1016/j.ocemod.2017.11.008

Wang, T. Y., Gille, S. T., Mazloff, M. R., Zilberman, N., & Du, Y. (2018). Numerical simulations to project Argo float positions in the mid-depth and deep southwest Pacific. *Journal of Atmospheric and Oceanic Technology*, *35*, 1425–1440. https://doi.org/10.1175/JTECH-D-17-0214.1

Wang, T., Gille, S. T., Mazloff, M. R., Zilberman, N., & Du, Y. (2019). Data from: Eddy-induced acceleration of Lagrangian floats. UC San Diego Library Digital Collections https://doi.org/10.6075/J0QR4VGP

Wijffels, S. E., Toole, J. M., & Davis, R. (2001). Revisiting the South Pacific subtropical circulation: A synthesis of World Ocean Circulation Experiment observations along 32°S. *Journal of Geophysical Research*, *106*, 19,481–19,513. https://doi.org/10.1029/1999JC000118

Williams, R. G., Wilson, C., & Hughes, C. W. (2007). Ocean and atmosphere storm tracks: The role of eddy vorticity forcing. *Journal of Physical Oceanography*, *37*, 2267–2289. https://doi.org/10.1175/JPO3120.1

Wolff, J.-O., Maier-Reimer, E., & Olbers, D. J. (1991). Wind-driven flow over topography in a zonal β-plane channel: A quasi-geostrophic model of the Antarctic Circumpolar Current. *Journal of Physical Oceanography*, *21*(2), 236–264. https://doi.org/10.1175/1520-0485(1991)021<0236:WDFOTI>2.0.CO;2

Zilberman, N., Roemmich, D., & Gille, S. T. (2017). The East Pacific Rise Current: Topographic enhancement of the interior flow in the South Pacific Ocean. *Geophysical Research Letters*, *44*, 277–285. https://doi.org/10.1002/2016GL069039